Sensors and Materials, Vol. 35, No. 5 (2023) 1587–1598
MYU Tokyo

S & M 3272

Vector-controlled Permanent Magnet Synchronous Motor Drive Speed Identification Using General Regression Neural Network

Yung-Chang Luo,* Hao-You Huang, Bo-Wei Chen, and Ying-Piao Kuo

Department of Electrical Engineering, National Chin-Yi University of Technology,
No. 57, Sec. 2, Zhongshan Rd, Taiping Dist, Taichung 41170, Taiwan (ROC)

(Received August 1, 2022; accepted April 20, 2023)

Keywords: vector control, permanent magnet synchronous motor (PMSM) drive, speed adjustment, general regression neural network (GRNN), particle swarm optimization (PSO) algorithm

In this work, we established a speed identification scheme for the surface-mounted vector-controlled permanent magnet synchronous motor (PMSM) drive. The decoupled vector-controlled PMSM drive was developed using the stator current and voltage. The speed loop and two-axis stator current loops were designed in accordance with this decoupling mathematical model. Hall effect current sensors were used to detect the PMSM currents. A general regression neural network (GRNN) was used to develop the speed identification scheme, and smooth curve adaptation of the pattern layer was used in the modified particle swarm optimization (PSO) algorithm. The two-axis stator current controllers and speed controller were designed using the root locus and Bode plot. The MATLAB\Simulink® toolbox was used to establish the simulation scheme and all control algorithms were realized using a TI DSP 6713-and-F2812 control card. Simulation and experimental results, including the estimated rotor speed, stator current, estimated electromagnetic torque, and the stator flux locus, confirmed the effectiveness of the proposed approach.

1. Introduction

The development of electric vehicles and precision machines demands a large number of energy-saving high-performance drives. Only the permanent magnet synchronous motor (PMSM) rotor has high-permeability permanent magnets without winding copper loss, making the PMSM drives widely used in today's intelligent machines. However, the coupling and time-varying mathematical model makes the control of PMSM more complicated than that of DC motors. According to the vector-controlled theory of AC motors,[1] the complicated mathematical model of a PMSM is separated into the torque-current and flux-current components through coordinate transformation, which are orthogonal to each other, and then the maximum torque-to-current ratio of a PMSM is achieved. A traditional vector-controlled PMSM drive requires an encoder to detect the shaft position. However, such a sensor reduces the robustness of the PMSM drive and is unsuitable for use in a hostile environment. Hence, the development of speed

*Corresponding author: e-mail: luoyc@ncut.edu.tw
https://doi.org/10.18494/SAM4067

ISSN 0914-4935

identification techniques in place of this position sensor is required for vector-controlled PMSM drives. Some speed identification methods for vector-controlled PMSM drives have been developed: speed identification using the extended Kalman filter,[2–5] speed determination by adopting adaptive control or the optimal control theory,[6–8] speed estimation based on the electromotive force or flux of the motor,[9–11] and speed identification scheme designed with a high-frequency signal injection and fuzzy logic control.[12–14] In this research, a speed identification scheme was established using the general regression neural network (GRNN) to improve the speed identification using a small amount of training data.[15] Electromagnetic Hall effect currents were used to detect the stator current for the implementation of the speed adjustment scheme.

This paper comprises six sections. In Sect. 1, we present the research motivation and background, and review the literature on speed identification methods for vector-controlled PMSM drives. In Sect. 2, the establishment of the decoupled vector-controlled PMSM drive is described. The details of the design of the speed identification procedure of GRNN for the vector-controlled PMSM drive are given in Sect. 3. In Sect. 4, we explain in detail the smooth curve adaptation of the pattern layer using the modified particle swarm optimization (PSO) algorithm. Sections 5 and 6 cover the experimental setup and results, discussion, and conclusions.

2. Vector-controlled PMSM Drive

Suppose the permanent magnets are arranged on the surface of the rotor without damping winding and the magnetic axis of the permanent magnet is consistent with the *d*-axis of the rotor shaft. The two-axis stator current state matrix of a PMSM in the synchronous reference coordinate frame is given by [16]

$$\begin{bmatrix} pi_{ds}^{e} \\ pi_{qs}^{e} \end{bmatrix} = \begin{bmatrix} -R_s/L_s & \omega_e \\ -\omega_e & -R_s/L_s \end{bmatrix} \begin{bmatrix} i_{ds}^{e} \\ i_{qs}^{e} \end{bmatrix} + \frac{1}{L_s} \begin{bmatrix} v_{ds}^{e} \\ v_{qs}^{e} - \omega_e \lambda_F \end{bmatrix}, \tag{1}$$

where $p = d/dt$ is the differential operator, j stands for the imaginary part, $\vec{i}_s^{\,e} = i_{ds}^{e} + ji_{qs}^{e}$ is the stator current, $\vec{v}_s^{\,e} = v_{ds}^{e} + jv_{qs}^{e}$ is the stator voltage, R_s and L_s are the resistance and inductance of the stator, respectively, λ_F is the equivalent rotor magnet flux produced by the permanent magnet of the rotor, and ω_e is the speed of the synchronous reference coordinate frame.

An inspection of the first row of the state equation in Eq. (1) shows that the second term on the right side is a coupling component in relation to the *q*-axis stator current. Furthermore, an inspection of the second row of Eq. (1) shows that the first and fourth terms on the right side are the coupling components related to the *d*-axis stator current and rotor magnet flux, respectively. These coupling components define the two-axis stator voltage feed-forward compensation matrix as

$$\begin{bmatrix} v_{ds\_comp}^{e} \\ v_{qs\_comp}^{e} \end{bmatrix} = \begin{bmatrix} -\omega_e L_s i_{qs}^{e} \\ \omega_e L_s i_{ds}^{e} + \omega_e \lambda_F \end{bmatrix}. \tag{2}$$

Hence, the two-axis stator current state matrix is decoupled from Eq. (1) to Eq. (3)

$$\begin{bmatrix} p i_{ds}^{e} \\ p i_{qs}^{e} \end{bmatrix} = \begin{bmatrix} -R_s/L_s & 0 \\ 0 & -R_s/L_s \end{bmatrix} \begin{bmatrix} i_{ds}^{e} \\ i_{qs}^{e} \end{bmatrix} + \frac{1}{L_s} \begin{bmatrix} v_{ds}^{e'} \\ v_{qs}^{e'} \end{bmatrix}, \tag{3}$$

where $v_{ds}^{e'}$ and $v_{qs}^{e'}$ are the outputs of the two-axis stator current controllers. The voltage command matrix of the two-axis stator current control loops is expressed as

$$\begin{bmatrix} v_{ds}^{e^*} \\ v_{qs}^{e^*} \end{bmatrix} = \begin{bmatrix} v_{ds}^{e'} \\ v_{qs}^{e'} \end{bmatrix} + \begin{bmatrix} v_{ds\_comp}^{e} \\ v_{qs\_comp}^{e} \end{bmatrix}, \tag{4}$$

where $v_{ds}^{e^*}$ and $v_{qs}^{e^*}$ are the voltage commands of the *d*-axis and *q*-axis stator current control loops, respectively. The resulting electromagnetic torque of a PMSM is derived using

$$T_e = (P/2)\lambda_F i_{qs}^{e}, \tag{5}$$

where P denotes the PMSM pole numbers. An inspection of Eq. (5) shows that the equivalent rotor magnet flux λ_F and the *q*-axis stator current i_{qs}^{e} are orthogonal to each other, the maximum torque-to-current ratio is achieved in the vector-controlled PMSM drive, and the electromagnetic torque is dominated by the *q*-axis stator current. The mechanical equation of the motor is obtained as

$$T_e - T_L = B_m \omega_{rm} + J_m p \omega_{rm}, \tag{6}$$

where T_L is the load torque, B_m and J_m respectively are the viscous friction coefficient and the motor inertia, $\omega_{rm} = (2/P)\omega_r$ is the mechanical speed of the motor rotor shaft, and ω_r is the electric speed of the rotor.

Using the first and second rows of Eq. (3), the plant transfer functions of the *d*-axis and *q*-axis stator current control loops are respectively given by

$$G_{plant\_i_{ds}}(s) = \frac{1/L_s}{s + R_s/L_s}, \tag{7}$$

$$G_{plant\_i_{qs}}(s) = \frac{1/L_s}{s + R_s/L_s}, \tag{8}$$

where s is the Laplace operator. Because the bandwidth of the inner q-axis stator current control loop is much higher than that of the outer speed control loop, the closed-loop gain of the q-axis stator current control loop can be regarded as one unit. According to Eq. (6) and the definition of the torque error ($\Delta T_e = T_e - T_L$), the plant transfer function of the speed control loop is given by

$$G_{plant\_speed}(s) = \frac{1/J_m}{s + B_m/J_m}. \tag{9}$$

Figure 1 shows the decoupled control block diagram of the vector-controlled PMSM drive. Here, K_{ps} and K_{is} are the proportional and integral gains of the speed controller, K_{pd} and K_{id} are the proportional and integral gains of the d-axis stator current controller, and K_{pq} and K_{iq} are the proportional and integral gains of the q-axis stator current controller, respectively. Because the rotor flux is a permanent magnet, the d-axis stator current command is set as 0.

Here, the speed controller and the d-axis and q-axis stator current controllers were designed using the root locus and Bode plot. Table 1 shows the proportional gain (K_p), integral gain (K_i), and bandwidth ($B.W$) for the three control loops.

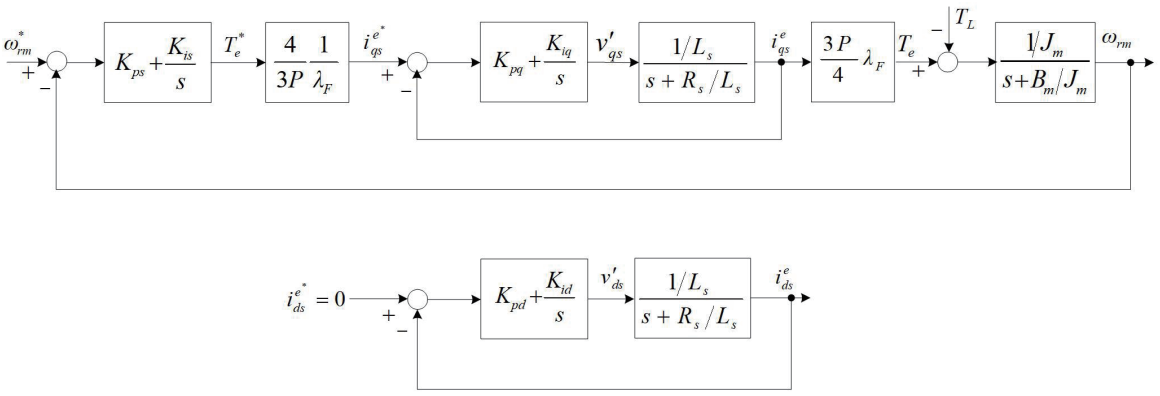

Fig. 1. Block diagram of the decoupling vector-controlled PMSM drive.

Table 1
Controller parameters and bandwidth.

Controller type	K_p	K_i	$B.W$
d-axis stator current	18	39600	420
q-axis stator current	16	36000	413
speed	4	100	5.56

3. Speed Identification Scheme Based on GRNN

In this study, the feedback speed signal of the traditional vector-controlled PMSM drive is replaced by a predicted speed. This speed identification scheme was developed based on GRNN. GRNN can be constructed as a multiple regression adjustment model with multiple inputs and multiple outputs. It can also be constructed as an automatic predictive model with high-dimensional nonlinear best input and output mapping relationships.[17,18] In this system, the training datasets of GRNN were obtained from the traditional vector-controlled PMSM drive. Here, the two-axis stator voltage (v_{ds}^s, v_{qs}^s) and two-axis stator current (i_{ds}^s, i_{qs}^s) in the stationary reference coordinate frame were selected as inputs, the synchronous position angle (θ_e) was selected as the output, and the smooth curve adaptation of the pattern layer was used in the modified PSO algorithm.[19] GRNN consists of the input layer, pattern layer, summation layer, and output layer, as shown in Fig. 2.

3.1 Input layer

In the input layer of the proposed speed identification GRNN model, the input datasets are $[v_{ds}^s, v_{qs}^s, i_{ds}^s, i_{qs}^s]$. The weight matrix between the input layer and the pattern layer is set as

$$w_{nk} = \left[\frac{v_{ds}^s(n)}{v_{ds\_\max}^s}, \frac{v_{qs}^s(n)}{v_{qs\_\max}^s}, \frac{i_{ds}^s(n)}{i_{ds\_\max}^s}, \frac{i_{qs}^s(n)}{i_{qs\_\max}^s} \right], \quad w_{nk} \in [0,1], \tag{10}$$

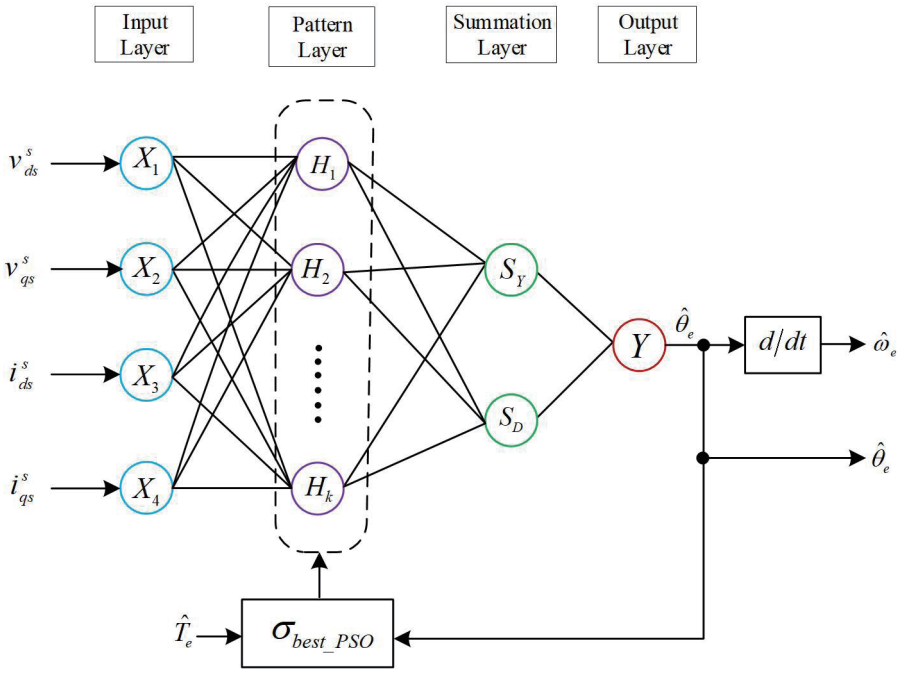

Fig. 2. (Color online) Speed identification scheme based on GRNN.

where $[v_{ds\_\max}^{s}, v_{qs\_\max}^{s}, i_{ds\_\max}^{s}, i_{qs\_\max}^{s}]$ is the maximum value of $[v_{ds}^{s}, v_{qs}^{s}, i_{ds}^{s}, i_{qs}^{s}]$, n = 1, 2, ..., N, and N is the number of training datasets. The normalized training database was acquired from the traditional vector-controlled PMSM drive.

3.2 Pattern layer

The number of pattern layers is determined by the training objects. More complex training objects require more pattern layers and, consequently, more computational burden. The pattern layer is approximated using a Gaussian function as

$$H_k = \exp\left[-\sum_{n=1}^{N}\frac{(x_k - p_k)^2}{2\sigma_n}\right], \tag{11}$$

where x_k is the input of the Gaussian function, p_k is the training database of the GRNN, k = 1, 2, 3, 4, and σ_n denotes the smoothing parameters that can be adjusted by the optimization algorithm. In this study, the modified PSO was used to adjust the smoothing parameters.

3.3 Summating layer

The summating layer comprises two operations. The first operation is summing all neurons in the pattern layer as expressed by Eq. (12). The other operation is multiplying each layer of the datasets by the output of the training datasets. The sum of the product is given by Eq. (13).

$$S_D = \sum H_k, \tag{12}$$

$$S_Y = \sum H_k Y_k. \tag{13}$$

Here, Y_k is the output of the training datasets.

3.4 Output layer

The output layer is obtained by dividing Eq. (13) by Eq. (12) and normalizing the result, as given by Eq. (14). In this study, the output layer provides the estimated synchronous position angle ($\hat{\theta}_e$). By differentiating the estimated synchronous position angle and multiplying the result by 2/P, the estimated rotor shaft speed ($\hat{\omega}_{rm}$) is then obtained, as shown in Fig. 2.

$$Y = \frac{S_Y}{S_D} Y_{max} \tag{14}$$

Here, $Y = \hat{\theta}_e$ and Y_{max} is the maximum of the training datasets.

4. Smooth Curve Adaptation of Pattern Layer Using Modified PSO Algorithm

The modified PSO was used to achieve smooth curve adaptation of the pattern layer because the algorithm is easily implemented and suitable for time-varying conditions. The smooth curve adaptation using the modified PSO is expressed as

$$\Delta\sigma_g^{p+1} = \Delta\sigma_g^p + \gamma_1 \cdot rand_1 \cdot (\sigma_{best\_g} - \sigma_g^p) + \gamma_2 \cdot rand_2 \cdot (\sigma_{best} - \sigma_g^p), \tag{15}$$

$$\gamma_1 = (\beta_1 - \alpha_1)\frac{p}{p_{max}} + \alpha_1, \tag{16}$$

$$\gamma_2 = (\beta_2 - \alpha_2)\frac{p}{p_{max}} + \alpha_2, \tag{17}$$

$$\sigma_g^{p+1} = \sigma_g^p + \Delta\sigma_g^{p+1}, \tag{18}$$

where g = 1, 2, ..., G is the number of particle swarms, p = 1, 2, ... is the number of iterations, $p_{\max}$ is the maximum number of iterations, σ_{best} is the best solution at the $p-1$th iteration, $\sigma_{\text{best\_}g}$ is the best solution of the g particle at the pth iteration, $rand_1 \in [0, 1]$ and $rand_2 \in [0, 1]$ are random, γ_1 and γ_2 are adjustable time-varying acceleration parameters, γ_1 (individual parameter) is decreased from β_1 = 2.5 to α_1 = 0.5, γ_2 (swarm parameter) is increased from β_2 = 0.5 to α_2 = 2.5, and $\Delta\sigma_g^{p+1}$ (time-varying adjustment parameter) corresponds to each travel distance of the particle swarm. In the initial search, $\Delta\sigma_g^{p+1}$ allows each particle to reach the target as soon as possible to avoid a local search. When approaching the target, the travel distance is reduced to search the global best solution. In the learning process, the best solution and learning experience of each iteration are retained, the optimal smooth curve adaptation can be quickly achieved, and the best parameters with adaptive learning and automatic decision-marking are obtained. Figure 3 shows the flow chart of the proposed modified PSO smooth curve adaptation.

Figure 4 shows the block diagram of the proposed speed identification vector-controlled PMSM drive using the GRNN, which includes the speed controller, q-axis and d-axis stator current controllers, d-axis and q-axis stator voltage decoupling, coordinate transformation between the two-axis synchronous reference frame and two-axis stationary reference frame ($2^e \Rightarrow 2^s$, $2^e \Leftarrow 2^s$), coordinate transformation between the three-phase system and two-axis stationary reference frame ($2^s \Rightarrow 3$, $2^s \Leftarrow 3$), and the GRNN rotor speed identification scheme. In this system, the speed controller and d-axis and q-axis stator current controllers were designed using the root locus and Bode plot, and the smooth curve adaptation of the pattern layer was used in the modified PSO algorithm.

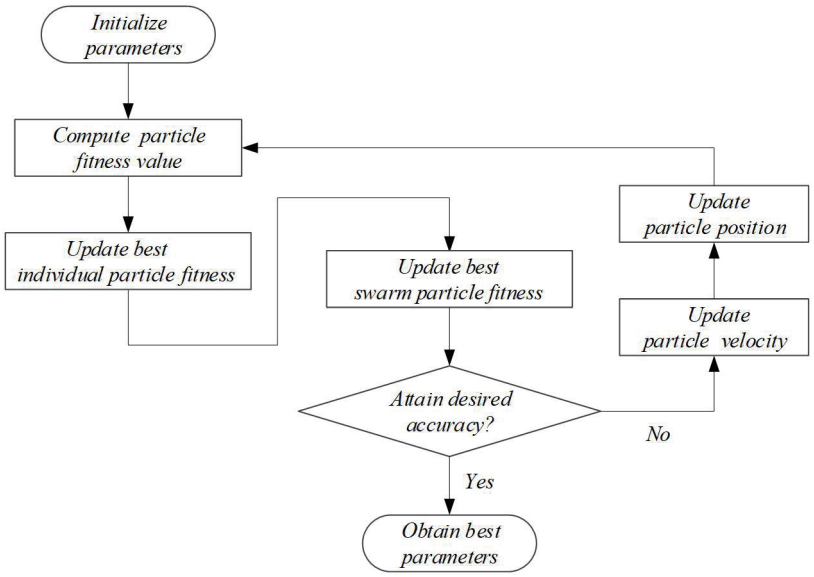

Fig. 3. Flow chart of proposed pattern layer smooth curve adaption using modified PSO.

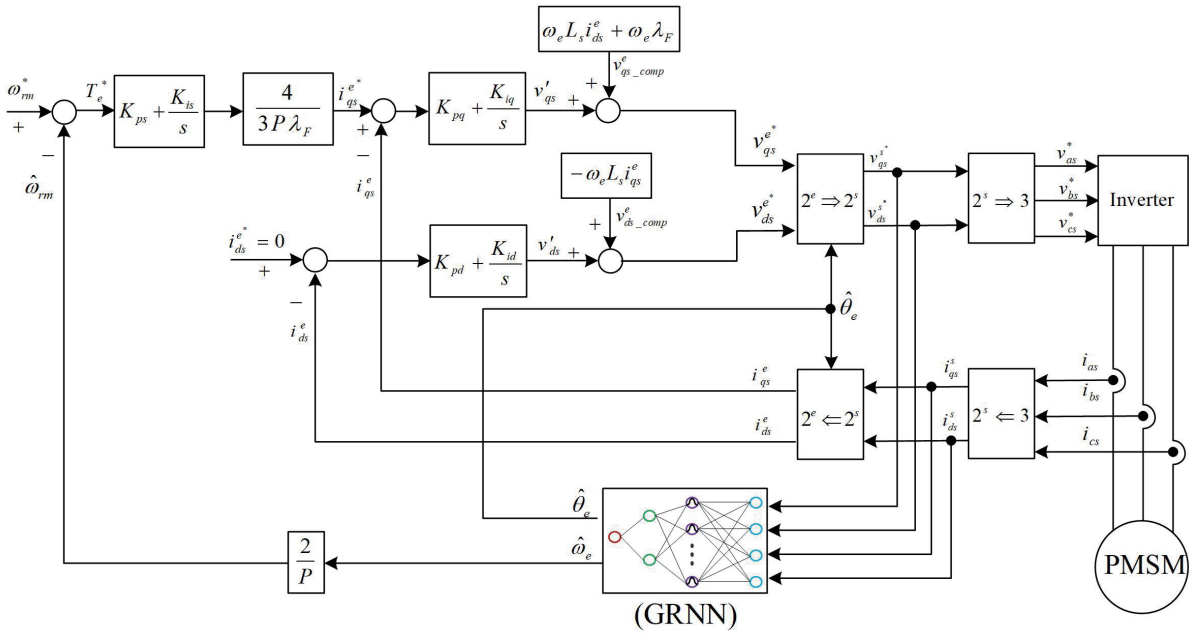

Fig. 4. (Color online) Speed identification vector-controlled PMSM drive based on GRNN.

5. Experimental Setup and Results

A 3-phase, 220 V, 0.75 kW, Y-connected, standard surface-mounted PMSM is used as the controlled plant for experimentation to confirm the effectiveness of the proposed speed

identification vector-controlled PMSM drive based on GRNN. In a running cycle, the speed command is designed as follows: forward direction acceleration from $t = 0$ to $t = 1$ s; forward direction steady-state running over $1 \leq t \leq 4$ s; forward direction braking to reach zero speed in the interval $4 \leq t \leq 5$ s; reverse direction acceleration from $t = 5$ to $t = 6$ s; reverse direction steady-state running over $6 \leq t \leq 9$ s; and reverse direction braking to reach zero speed in the interval $9 \leq t \leq 10$ s.

Figures 5 and 6 show the simulated and measured responses with 3 N-m load for reversible steady-state speed commands at 1800 rev/min. Each figure contains six responses: (a) command

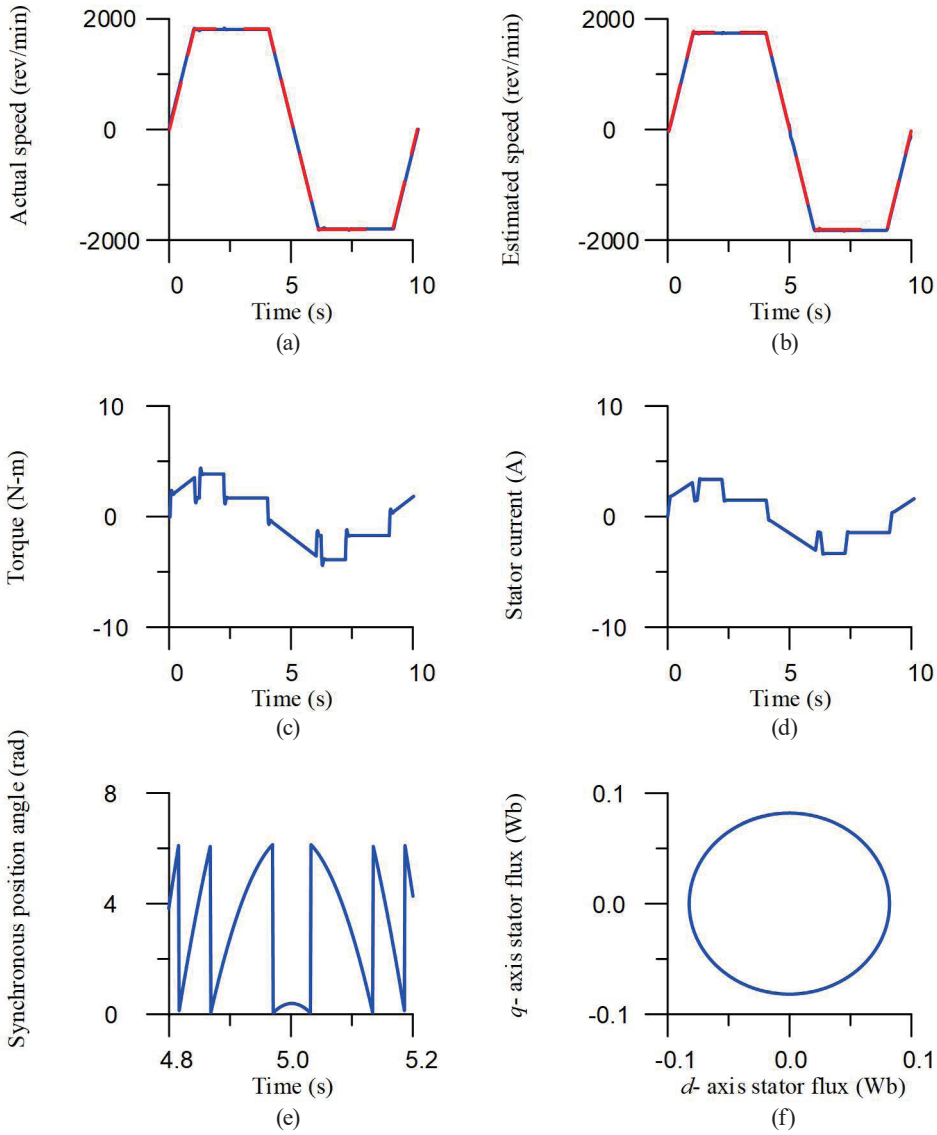

Fig. 5. (Color online) Simulated responses of the proposed speed identification vector-controlled PMSM drive based on GRNN with 3 N-m load for reversible steady-state speed command of 1800 rev/min. (a) Actual rotor speed, (b) estimated rotor speed, (c) electromagnetic torque, (d) stator current, (e) synchronous position angle, and (f) stator flux locus.

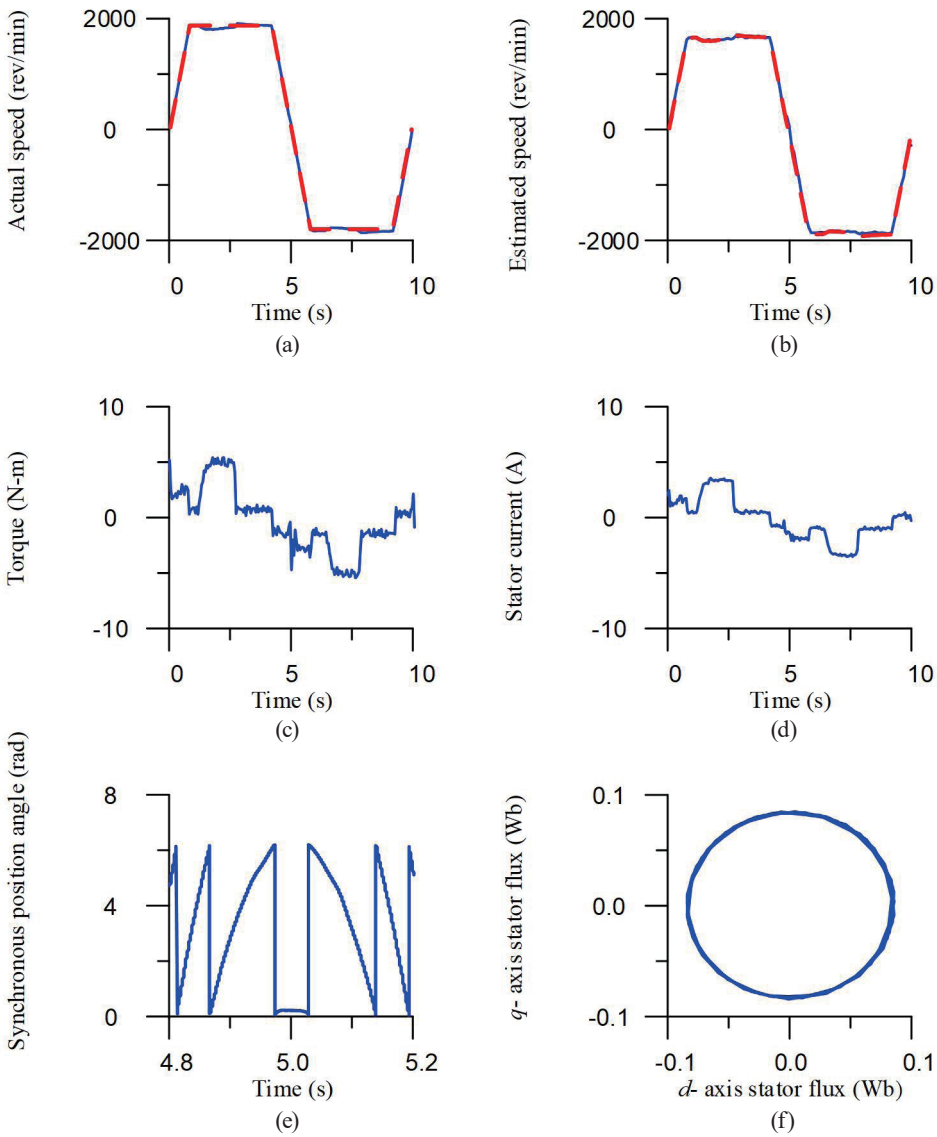

Fig. 6. (Color online) Experimental responses of the proposed speed identification vector-controlled PMSM drive based on GRNN with 3 N-m load for reversible steady-state speed command of 1800 rev/min. (a) Actual rotor speed, (b) estimated rotor speed, (c) electromagnetic torque, (d) stator current, (e) synchronous position angle, and (f) stator flux locus.

(dashed line) and actual (solid line) rotor speed; (b) command (dashed line) and estimated (solid) rotor speed; (c) electromagnetic torque; (d) stator current; (e) synchronous position angle; and (f) stator flux locus (q-axis vs d-axis).

From the simulated and measured responses, the accurate estimation of the rotor speed was attained using the GRNN scheme. The synchronous position angle and stator flux locus confirmed that the coordinate transformation between the synchronous reference frame and the stationary reference frame was effected. Good responses for the stator current and electromagnetic torque were also effectively achieved. Hence, the proposed speed identification

vector-controlled PMSM drive using GRNN showed that the desired performance can be acquired.

6. Conclusions

A speed identification scheme based on the GRNN was developed for vector-controlled PMSM drives. The decoupled vector-controlled PMSM drive was established using the stator current and voltage. The root locus and Bode plot were used to design the speed controller and the *d*-axis and *q*-axis stator current controllers. The GRNN was used to design the speed identification scheme, and the smooth curve adaptation of the pattern layer was used in the modified PSO algorithm. The three-phase stator currents for implementing the speed identification vector-controlled PMSM drive based on the GRNN scheme were provided by the Hall effect current sensors. Simulation and experimental results for reversible steady-state speed commands under a load condition confirmed the promising performance of the proposed speed identification method for the vector-controlled PMSM drive.

References

1 Y. C. Luo, B. W. Chen, W. C. Pu, and N. S. Pai: Sens. Mater. **32** (2020) 239. https://doi.org/10.18494/SAM.2020.2574
2 R. Cao, N. Jiang, and M. Lu: IEEE Trans. Ind. Electro. **67** (2020) 5971. https://doi.org/10.1109/TIE.2019.2950865
3 F. Toso, D. D. Rù, P. Alotto, and S. Bolognani: IEEE Trans. Pow. Electro. **34** (2019) 580. https://doi.org/10.1109/TPEL.2018.2823905
4 S. M. Saghaiannezhad and A. Rashidi: Proc. 2020 11th Power Electronics Drive Systems Technologies Conf. (PEDSTC, 2018) 1–5. https://doi.org/10.1109/PEDSTC49159.2020.9088400
5 M. S. Termizi, J. M. Lazi, Z. Ibrahim, M. H. N. Talib, M. J. A. Aziz, and S. M. Ayob: Proc. 2017 IEEE Energy Conversion Conf. (CENCON, 2017) 145–150. https://doi.org/10.1109/CENCON.2017.8262474
6 Q. An and L. Sun: Proc. 2008 IEEE Vehicle Power Propulsion Conf. (VPPC, 2008) 1–6. https://doi.org/10.1109/VPPC.2008.4677634
7 P. V. Medagam, T. Yucelen, and F. Pourboghrat: Proc. 2009 American Control Conf. (ACC, 2009) 3866–3871. https://doi.org/10.1109/ACC.2009.5160104
8 M. Comanescu: Proc. 2020 Int. Sym. Power Electronics Electrical Drives Automation Motion (SPEEDAM, 2020) 213–218. https://doi.org/10.1109/SPEEDAM48782.2020.9161899
9 S. Huang, Q. Pu, J. Gao, T. Liu, L. Xiao, and J. Kuang: Proc. 2011 Int. Conf. Power Engineering Energy Electrical Drives (PEEED, 2011) 1–6. https://doi.org/10.1109/PowerEng.2011.6036492
10 C. L. Baratieri and H. Pinheiro: Proc. 2014 40th IEEE Industrial Electronics Society Conf. (IECON, 2014) 621–627. https://doi.org/10.1109/IECON.2014.7048565
11 M. Comanescu: Proc. 2012 38th IEEE Industrial Electronics Society Conf. (IECON, 2014) 3670–3675. https://doi.org/10.1109/IECON.2012.6389308
12 Y. Yang and H. Gao: Proc. 2009 IEEE Int. Electric Machine Drives Conf. (IEMDC, 2009) 514–520. https://doi.org/10.1109/IEMDC.2009.5075255
13 R. Kennel: Proc. 2010 12th Int. Optimization Electrical Electronic Equipment Conf. (OPTIM, 2010) 19–24. https://doi.org/10.1109/OPTIM.2010.5510480
14 J. L. F. Daya and V. Subbiah: Proc. 2010 2nd Int. Advanced Computer Control Conf. (ICACC, 2010) 14–18. https://doi.org/10.1109/ICACC.2010.5486774
15 Y. C. Luo, H. H. Zheng, C. H. Lin, and Y. P. Kuo: Sens. Mater. **33** (2021) 1955. https://doi.org/10.18494/SAM.2021.3271
16 C. H. Liu: Control of AC Electrical Machines (Tunghua, Taipei, 2008) 4th ed., Chap. 6 (in Chinese).
17 M. R. Noghondari and M. Rashidi: Proc. 39th Int. Universities Power Engineering Conf. (UPEC, 2004) 353–357.

18 J. Chen, Y. Chen, Z. Guo, and W. Qiu: Proc. 2020 Int. Computer Information and Big Data Applications Conf. (CIBDA, 2020). 204–207.
19 Y. C. Luo, X. H. Zheng, C. H. Liao, and Y. P. Kuo: Sens. Mater. **32** (2020) 1955. https://doi.org/10.18494/SAM.2020.2785